

Evolution of the Fermi surface of Weyl semimetals in the transition metal pnictide family

Z. K. Liu^{1,2,3†}, L. X. Yang^{4,5,6†}, Y. Sun^{7†}, T. Zhang^{4,5}, H. Peng⁵, H. F. Yang^{5,8}, C. Chen⁵, Y. Zhang⁶, Y. F. Guo^{1,2,5}, D. Prabhakaran⁵, M. Schmidt⁷, Z. Hussain⁶, S.-K. Mo⁶, C. Felser⁷, B. Yan^{1,2,7} and Y. L. Chen^{1,2,3,4,5*}

Topological Weyl semimetals (TWSs) represent a novel state of topological quantum matter^{1–4} which not only possesses Weyl fermions (massless chiral particles that can be viewed as magnetic monopoles in momentum space) in the bulk and unique Fermi arcs generated by topological surface states, but also exhibits appealing physical properties such as extremely large magnetoresistance and ultra-high carrier mobility^{5–8}. Here, by performing angle-resolved photoemission spectroscopy (ARPES) on NbP and TaP, we directly observed their band structures with characteristic Fermi arcs of TWSs. Furthermore, by systematically investigating NbP, TaP and TaAs from the same transition metal monpnictide family, we discovered their Fermiology evolution with spin-orbit coupling (SOC) strength. Our experimental findings not only reveal the mechanism to realize and fine-tune the electronic structures of TWSs, but also provide a rich material base for exploring many exotic physical phenomena (for example, chiral magnetic effects, negative magnetoresistance, and the quantum anomalous Hall effect) and novel future applications^{3,4,9–11}.

Three-dimensional (3D) topological Weyl semimetals (TWSs) represent a new state of quantum matter recently proposed with unusual electronic structures that resemble both a ‘3D graphene’ and a topological insulator (TI). On one hand, a TWS possesses bulk Weyl fermions, unique chiral particles that disperse linearly along all three momentum directions across a point—the Weyl point—which can be viewed as a magnetic monopole in momentum space¹². As a Weyl fermion possesses half the number of degrees of freedom as a Dirac fermion, they always appear in pairs (with opposite chirality) in materials^{1,3,4,12}. On the other hand, a TWS also possesses non-trivial topological surface states that form unique ‘Fermi arcs’^{1,3,4}—unusual Fermi surfaces (FSs) consisting of unclosed curves that start and end at Weyl points (Fig. 1b). The unusual bulk and surface electronic structure of 3D TWSs can give rise to many exotic phenomena, such as negative magnetoresistance, chiral magnetic effects, the quantum anomalous Hall effect, novel quantum oscillations (in magneto-transport) and quantum interference (in tunnelling spectroscopy)^{10,13–16}. In addition, appealing transport properties have also been discovered in some 3D TWS candidates, such as the ultra-high carrier mobility and extremely large magnetoresistance^{5–8}, making 3D TWSs not only ideal for fundamental research, but also promising materials for novel applications.

In comparison to 3D topological Dirac semimetals (TDSs; refs 17–20), which possess bulk Dirac fermions, 3D TWSs can be realized by breaking either time reversal symmetry (TRS) or inversion symmetry in 3D TDSs (refs 1–3,21,22)—thus a Dirac point can be split into a pair of Weyl points of opposite chirality. In the past few years, several compounds (for example, $\text{Y}_2\text{Ir}_2\text{O}_7$ (ref. 1) and HgCr_2Se_4 (ref. 2)) have been proposed to be TWS candidates with spontaneously broken TRS. Unfortunately, none have been experimentally confirmed so far.

On the other hand, recent theoretical investigations^{3,4,22} have indicated that various compounds with spontaneously broken inversion symmetry can also be TWS candidates, with a promising family of transition metal monpnictides (including NbP, NbAs, TaP and TaAs; refs 3,4). In this family of materials, a total of twelve pairs of Weyl points are predicted to exist within a 3D Brillouin zone (BZ), with each pair residing across one of the two crystalline mirror planes (Fig. 1a) and connected by unique surface Fermi arcs (Fig. 1b). In the formation of the TWS, the spin-orbit coupling (SOC) plays an essential role, and the splitting between the Weyl points and the Fermi arcs should increase with the strength of the SOC in different compounds (Fig. 1b)³, as confirmed by our *ab initio* calculations (Fig. 1c).

In this work, we first investigated the electronic structure of the TWS candidates NbP and TaP by angle-resolved photoemission spectroscopy (ARPES) (see Methods for details of the measurement) and observed the characteristic surface Fermi arcs in both compounds. The excellent agreement between our experiments and *ab initio* calculations (as well as other theoretical investigations^{3,4}) confirmed that NbP and TaP are TWSs. More importantly, we systematically studied the evolution of the band structures of NbP, TaP and another compound (TaAs) in the same family (which was recently confirmed as a TWS (refs 5,7,23–25)) and discovered a clear increase in the separation between the Weyl points and Fermi arcs from NbP to TaP, and to TaAs. Our result demonstrates for the first time the crucial effect of the SOC in the formation and fine-tuning of the electronic structure of TWSs, including the Fermi-arc splitting and Weyl point separation—which will facilitate the design of new TWS materials with tailored electronic properties.

The crystal structure of NbP and TaP are illustrated in Fig. 1d, showing they have the same crystal symmetry but slightly different lattice constants (NbP: $a = b = 3.33 \text{ \AA}$, $c = 11.37 \text{ \AA}$,

¹School of Physical Science and Technology, ShanghaiTech University, Shanghai 200031, China. ²CAS-Shanghai Science Research Center, 239 Zhang Heng Road, Shanghai 201203, China. ³Diamond Light Source, Didcot, Oxfordshire OX11 0QX, UK. ⁴State Key Laboratory of Low Dimensional Quantum Physics, Collaborative Innovation Center of Quantum Matter and Department of Physics, Tsinghua University, Beijing 100084, China. ⁵Physics Department, Oxford University, Oxford OX1 3PU, UK. ⁶Advanced Light Source, Lawrence Berkeley National Laboratory, Berkeley, California 94720, USA. ⁷Max Planck Institute for Chemical Physics of Solids, D-01187 Dresden, Germany. ⁸State Key Laboratory of Functional Materials for Informatics, SIMIT, Chinese Academy of Sciences, Shanghai 200050, China. [†]These authors contributed equally to this work. *e-mail: yulin.chen@physics.ox.ac.uk

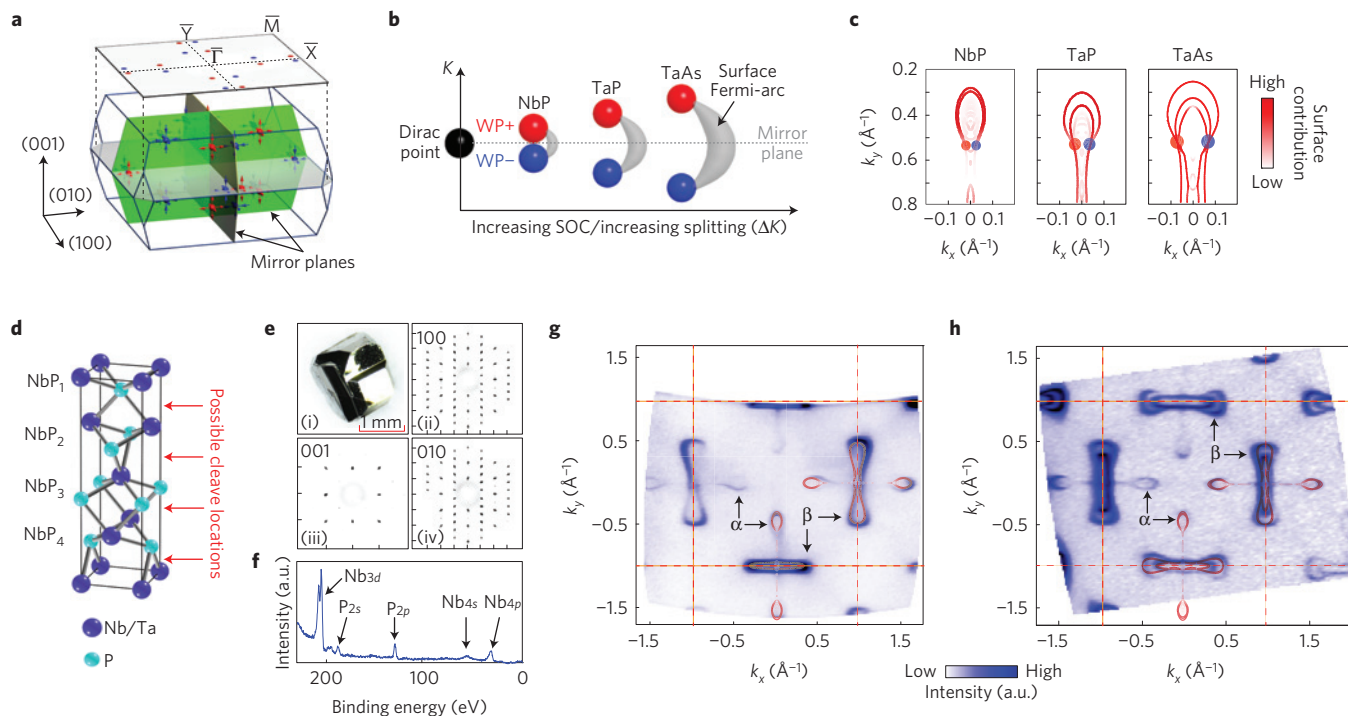


Figure 1 | Properties of TWSs and characterization of NbP/TaP single crystals. **a**, Schematic of bulk and (001) surface Brillouin zones (BZs) of transition metal monopnictides. Twelve pairs of Weyl points predicted by theoretical investigations^{3,4} (see text for details) are marked as red and blue dots. Three mirror planes of the bulk BZ are indicated. **b**, Illustration of the separation of a pair of Weyl points (with opposite chirality, marked as WP+ and WP-) controlled by the SOC strength in different compounds of the family. The dotted line represents the crystalline mirror plane, and the grey arcs represent the surface Fermi arcs that connect the two Weyl points. **c**, *Ab initio* calculations show the Weyl points and surface Fermi arcs of NbP, TaP and TaAs, respectively. The colour bar shows the surface contribution of the FS (white/0% to red/100%); the same scale is used for Figs 2–4. **d**, Crystal structure of NbP/TaP, showing the ...A–B–C–D... stacking of NbP/TaP layers. Red arrows indicate interlayer positions where cleavage possibly takes place. **e**, (i) Image of NbP single crystals with the shiny flat surface used for ARPES measurements. (ii–iv) X-ray diffraction patterns from the (100), (001) and (010) directions. **f**, Core-level photoemission spectrum of NbP shows characteristic Nb (4s, 4p, 3d) and P (2s, 2p) peaks. **g**, Broad FS mapping of NbP shows excellent agreement with the *ab initio* calculations (overlapped red dotted plots). The orthogonal spoon-like and bowtie-like FS pockets are denoted as α - and β -FSs, respectively. Blue colour bar indicates the ARPES spectra intensity (the same scale is used for Figs 2–4). **h**, Broad FS mapping of NbP from two adjacent cleaved NbP layers shows the mixing of two sets of electronic structures rotated by 90° with respect to each other. The orthogonal spoon-like and bowtie-like FS pockets are denoted as α - and β -FSs, respectively.

TaP: $a=b=3.33 \text{ \AA}$, $c=11.39 \text{ \AA}$). Taking NbP as an example, its tetragonal unit cell is formed by four NbP layers with a repeating ...–NbP₁–NbP₂–NbP₃–NbP₄–... stacking sequence without inversion symmetry (Fig. 1d)²⁶. As the interlayer distance between the Nb and P planes along the c -direction ($0.167c/1.899 \text{ \AA}$) is about twice as large as their intra-layer distance ($0.083c/0.944 \text{ \AA}$), the crystal can be naturally cleaved between adjacent NbP layers (Fig. 1d and Supplementary Fig. 1) for the ARPES measurements (Fig. 1e(i)). The high quality of the NbP crystals (see Methods for details on sample synthesis) is verified by the sharp X-ray diffraction patterns from all three crystalline orientations (Fig. 1e(ii–iv)), and the core-level photoemission spectrum (Fig. 1f), which clearly indicates different characteristic Nb (4s, 4p, 3d) and P (2s, 2p) peaks. The overall electronic structure of NbP is captured in Fig. 1g by a broad momentum-space mapping, which shows the global FS topology across multiple BZs of the (001) surface that agrees excellently with our *ab initio* calculations (overlapped dotted plots). The FS is comprised of two cross-shape features centred at the \bar{X} and \bar{Y} points, each containing two sets of orthogonal FS pockets: the spoon-like and the bowtie-like pockets marked as α -FS and β -FS in Fig. 1g, respectively. As the broken Nb–P bonds are along orthogonal directions between adjacent cleaved NbP layers (see Supplementary Fig. 1 for details), ARPES measurements sometimes show electronic structures from both kinds of layers (Fig. 1h, also see Supplementary Figs 1 and 2 for more discussion).

In Fig. 2, we illustrate the detailed electronic structure of NbP. The stacking plots of constant-energy contours at different binding energies (Fig. 2a) show the electronic structure evolution from the isolated cross-shape FSs centred at the \bar{X} and \bar{Y} points to a more complicated interconnected texture at higher binding energies. To compare with the *ab initio* calculations (see Methods for details), in Fig. 2b we present three side-by-side comparison examples which demonstrate broad agreement: both the spoon-like and bowtie-like FS pockets (Fig. 2b(i)) and their evolution to nested textures at higher binding energies (Fig. 2b(ii), (iii)) can be nicely reproduced by the calculation. Remarkably, the characteristic Fermi-arc type FS suggested by our *ab initio* calculation and previous theoretical investigations^{3,4} clearly shows up as the spoon-like FSs, as we will discuss in detail later.

In addition to the Fermiology and constant-energy contours, the band structure for both the spoon and bowtie-like FSs with overlaid dispersions from calculation are presented as a 3D plot in Fig. 2c, which again shows excellent agreement. In fact, the overall agreement between experiment and theory can be seen throughout the whole BZ, as illustrated by the comparison in Fig. 2d. Finally, to verify the surface nature of the spoon-like and bowtie-like FSs (as suggested by our *ab initio* calculations and refs 3,4), we carried out photon-energy-dependent ARPES measurements²⁷ to investigate the k_z dispersion of these bands. In Fig. 2e, the ARPES spectra over a broad photon energy range

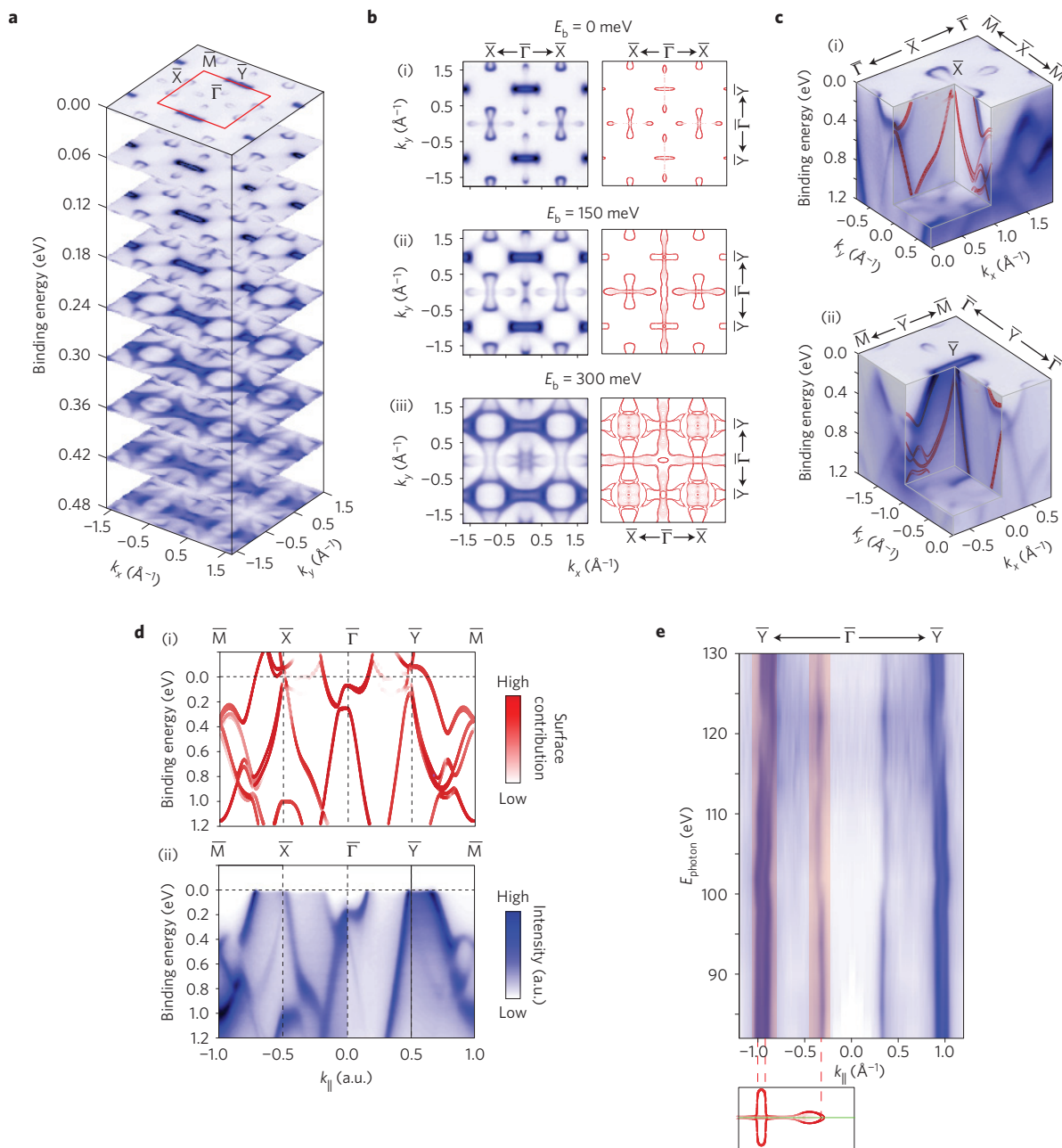


Figure 2 | Overall electronic structure of NbP. **a**, Stacking plots of constant-energy contours at different binding energies showing the band structure evolution. Red square marks the first BZ. **b**, Side-by-side comparison of three constant-energy contours between experiments (left panels) and *ab initio* calculations (right panels) shows overall agreement. **c**, 3D intensity plots of the photoemission spectra around the \bar{X} (i) and \bar{Y} (ii) points illustrate the zoomed-in band structure for both the bowtie-like and spoon-like FSs with overlaid dispersions from calculation. **d**, Comparison of calculated (i) and experimental (ii) dispersions along the high-symmetry directions across the whole BZ ($\bar{M}-\bar{X}-\bar{\Gamma}-\bar{Y}-\bar{M}$). **e**, Plot of photoemission intensities at the Fermi energy (E_F) along the high-symmetry $\bar{Y}-\bar{\Gamma}-\bar{Y}$ direction (measurement position is along the green line marked on the FS in the lower panel) as a function of photon energy (82–130 eV), showing the k_z dispersion of different bands.

(52–130 eV) clearly demonstrate the absence of vertical dispersion (that is, no k_z -dispersion, more information of photon-energy-dependent measurements can be found in the Supplementary Information), proving their surface nature (the photon-energy-dependent measurement along both $\bar{\Gamma}-\bar{X}$ and $\bar{\Gamma}-\bar{Y}$ directions can be found in the Supplementary Information).

Similar measurements were also conducted on another member (TaP) of the same family of compounds. As can be seen in Fig. 3, the overall electronic structure, such as the FS topology, including the spoon-like and bowtie-like FS pockets (Fig. 3a,b), and the band dispersions along different directions (Fig. 3c,d), again show

excellent agreement with the *ab initio* calculations. The difference between the measured band structure of TaP (Fig. 3) and NbP (Fig. 2) is mainly quantitative: the bands that generate the spoon-like FS have larger splitting in TaP (as will be discussed later with Fig. 4).

The existence of Fermi arcs on the surface of TaP can also be verified by counting the number of FS crossings along a closed reference loop in the BZ (ref. 24) and obtaining an odd number of FS crossings (Fig. 3d). As shown in Fig. 3e, along the closed loop of $\bar{\Gamma}-\bar{X}-\bar{M}-\bar{\Gamma}$, we observe seven (an odd number) FS crossings in total, which confirms the existence of the Fermi arcs (further discussion and counting of the FS crossings in NbP can be found in

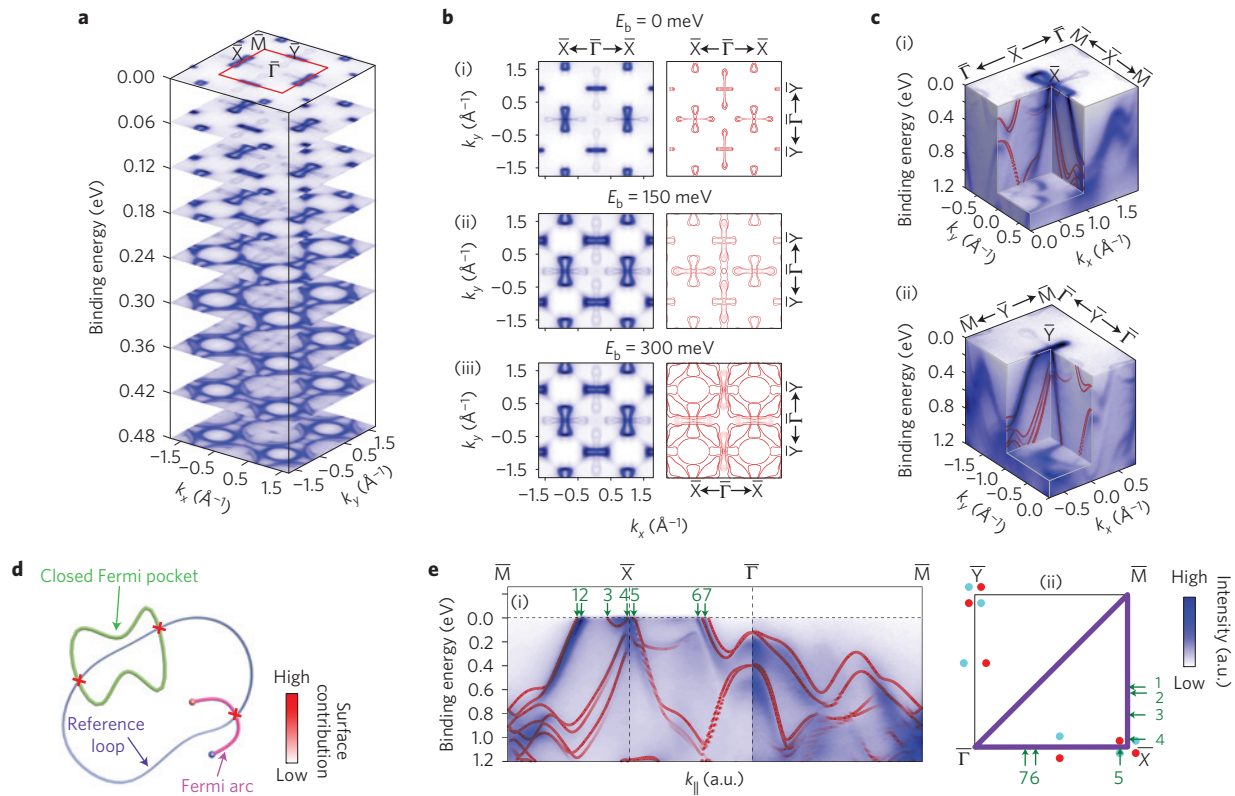


Figure 3 | Overall electronic structure of TaP. **a**, Stacking plots of constant-energy contours of the full BZ at different binding energies showing the band structure evolution. **b**, Comparison of three constant-energy contours at different binding energies between experiments (left panels) and *ab initio* calculations (right panels) shows excellent agreement. **c**, 3D intensity plots of the photoemission spectra around the \bar{X} (i) and \bar{Y} (ii) point illustrate the zoomed-in band structure for both the bowtie-like and spoon-like FSs with overlaid dispersions from calculation. **d**, Schematic of an arbitrary reference loop in the momentum space crossing a closed Fermi pocket and a broken Fermi arc, the crossing points are denoted by the red crosses. **e**, (i) Comparison of calculated and experimental high-symmetry cuts along a closed reference loop in the momentum space (\bar{M} - \bar{X} - $\bar{\Gamma}$ - \bar{M}). Green arrows denote the Fermi surface crossings. (ii) Schematic of the closed reference loop in the momentum space as well as the labelled positions of FS crossings along the loop. Coloured dots show the position of the Weyl points in the BZ.

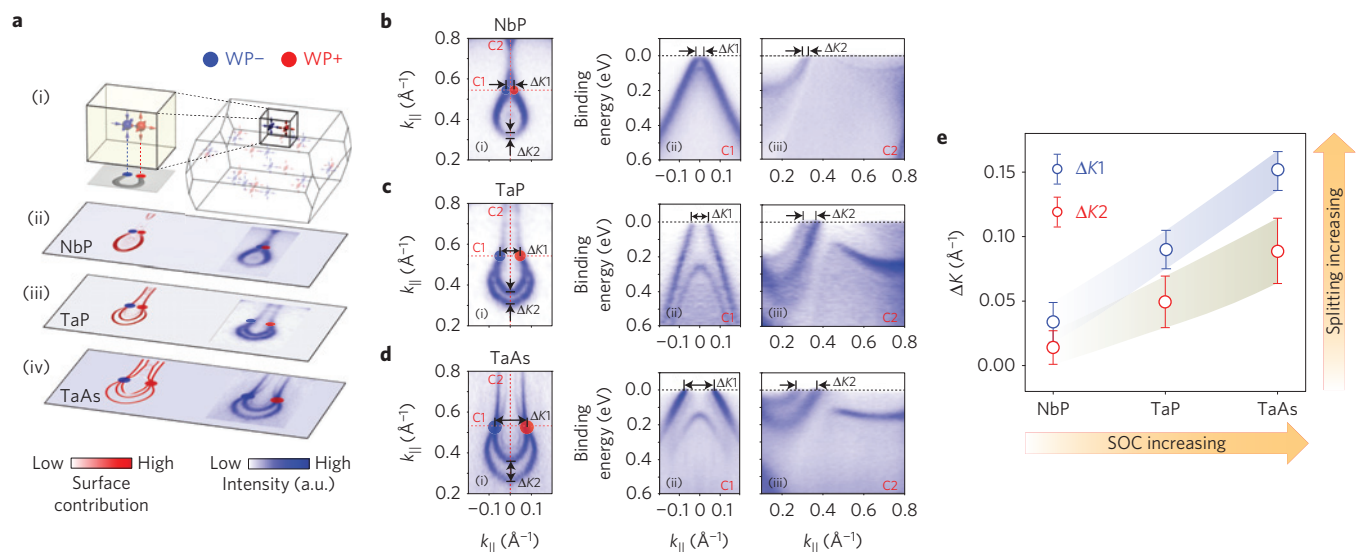


Figure 4 | Evolution of the band structure with SOC. **a**, (i) Schematic plot shows a pair of Weyl points projected to the (001) surface BZ and the Fermi arc (grey curves) connecting them. (ii-iv) Comparison of the calculated (left) and ARPES measurement (right) of the spoon-like FSs, showing good agreement. Red/blue dots denote the Weyl points of opposite chirality (labelled as WP+ and WP-). **b-d**, High-resolution ARPES measurements on the spoon-like FS (i) and associated band dispersions (ii,iii) for NbP, TaP and TaAs, respectively. The positions of the band dispersions presented in (ii,iii) are indicated by the red dotted lines in (i). $\Delta K1$ and $\Delta K2$ represent the separation between the Weyl points and Fermi arcs, respectively. **e**, Summary of the extracted $\Delta K1$ and $\Delta K2$ (from **b-d**) from the three compounds, plotted against the SOC strength. Error bars of $\Delta K1$ and $\Delta K2$ are estimated from the uncertainty in the fitting of the momentum distribution curves at E_F .

the Supplementary Information). In addition to the unique surface Fermi arc, we also carried out ARPES measurements with high photon energy to investigate the bulk Weyl fermions in TaP (see Supplementary Information).

After establishing the experimental band structures of NbP and TaP, we now focus on the characteristic spoon-like FS, which forms the Fermi arcs that connect the two Weyl points of opposite chirality, as suggested by recent theoretical investigations^{3,4} and our calculations (see Fig. 4a(i)). To investigate the evolution of Fermi arcs over different compounds in this transition metal monpnictide family, we also carried out ARPES experiments on TaAs (more details can be found in the Methods and Supplementary Information) in addition to NbP and TaP.

High-resolution momentum and energy measurements on the spoon-like FSs for all three compounds are summarized in Fig. 4—which can be nicely reproduced by our calculations (Fig. 4a), including each FS piece and its detailed shape, thus confirming the three compounds are TWSs as proposed³. The detailed FS topology and associated band dispersions are illustrated in Fig. 4b–d, indicating a clear increase of the separation between the Weyl points ($\Delta K1$ in panel (i) and (ii) of Fig. 4b–d) and the Fermi arcs ($\Delta K2$ in panel (i) and (iii) of Fig. 4b–d) from compound NbP to TaP, and on to TaAs. In Fig. 4e we collect the $\Delta K1$ and $\Delta K2$ values extracted and plot them against the SOC strength of the three compounds, clearly verifying their correspondence and showing that the SOC can act as an effective controlling parameter to tune the splitting of the Weyl points and Fermi arcs (further discussions can be found in the Supplementary Information).

Our systematic study on the electronic band structures of NbP, TaP and TaAs and observation of the characteristic surface Fermi arcs, together with the excellent agreement with the theoretical prediction^{3,4} and our detailed *ab initio* calculations, establish the first TWS family in transition metal monpnictides. This discovery and the SOC-controlled band structure and Fermiology tuning further pave the way for the exploration of novel phenomena and potential future applications in TWSs.

Methods

Methods and any associated references are available in the [online version of the paper](#).

Received 16 April 2015; accepted 24 September 2015;
published online 2 November 2015

References

1. Wan, X., Turner, A. M., Vishwanath, A. & Savrasov, S. Y. Topological semimetal and Fermi-arc surface states in the electronic structure of pyrochlore iridates. *Phys. Rev. B* **83**, 205101 (2011).
2. Xu, G., Weng, H., Wang, Z., Dai, X. & Fang, Z. Chern semimetal and the quantized anomalous Hall effect in HgCr_2Se_4 . *Phys. Rev. Lett.* **107**, 186806 (2011).
3. Weng, H., Fang, C., Fang, Z., Bernevig, A. & Dai, X. Weyl semimetal phase in non-centrosymmetric transition-metal monophosphides. *Phys. Rev. X* **5**, 011029 (2015).
4. Huang, S.-M. *et al.* A Weyl Fermion semimetal with surface Fermi arcs in the transition metal monpnictide TaAs class. *Nature Commun.* **6**, 7373 (2015).
5. Zhang, C. *et al.* Observation of the Adler–Bell–Jackiw chiral anomaly in a Weyl semimetal. Preprint at <http://arXiv.org/abs/1503.02630> (2015).

6. Shekhar, C. *et al.* Extremely large magnetoresistance and ultrahigh mobility in the topological Weyl semimetal NbP. *Nature Phys.* **11**, 645–649 (2015).
7. Huang, X. *et al.* Observation of the chiral-anomaly-induced negative magnetoresistance in 3D Weyl semimetal TaAs. *Phys. Rev. X* **5**, 031023 (2015).
8. Ghimire, N. J. *et al.* Magnetotransport of single crystalline NbAs. *J. Phys. Condens. Matter* **27**, 152201 (2015).
9. Yang, K.-Y., Lu, Y.-M. & Ran, Y. Quantum Hall effects in a Weyl semimetal: Possible application in pyrochlore iridates. *Phys. Rev. B* **84**, 075129 (2011).
10. Zyuzin, A. A. & Burkov, A. A. Topological response in Weyl semimetals and the chiral anomaly. *Phys. Rev. B* **86**, 115133 (2012).
11. Hosur, P. & Qi, X. Recent developments in transport phenomena in Weyl semimetals. *C. R. Phys.* **14**, 857–870 (2013).
12. Balents, L. Weyl electrons kiss. *Physics* **4**, 36 (2011).
13. Liu, C.-X., Ye, P. & Qi, X.-L. Chiral gauge field and axial anomaly in a Weyl semimetal. *Phys. Rev. B* **87**, 235306 (2013).
14. Landsteiner, K. Anomalous transport of Weyl fermions in Weyl semimetals. *Phys. Rev. B* **89**, 075124 (2014).
15. Potter, A. C., Kimchi, I. & Vishwanath, A. Quantum oscillations from surface Fermi arcs in Weyl and Dirac semimetals. *Nature Commun.* **5**, 6161 (2014).
16. Hosur, P. Friedel oscillations due to Fermi arcs in Weyl semimetals. *Phys. Rev. B* **86**, 195102 (2012).
17. Wang, Z. *et al.* Dirac semimetal and topological phase transitions in A_3Bi ($\text{A} = \text{Na}, \text{K}, \text{Rb}$). *Phys. Rev. B* **85**, 195320 (2012).
18. Liu, Z. K. *et al.* Discovery of a three-dimensional topological Dirac semimetal, Na_3Bi . *Science* **343**, 864–867 (2014).
19. Liu, Z. K. *et al.* A stable three-dimensional topological Dirac semimetal Cd_3As_2 . *Nature Mater.* **13**, 677–681 (2014).
20. Neupane, M. *et al.* Observation of a three-dimensional topological Dirac semimetal phase in high-mobility Cd_3As_2 . *Nature Commun.* **5**, 4786 (2014).
21. Burkov, A. A. & Balents, L. Weyl Semimetal in a topological insulator multilayer. *Phys. Rev. Lett.* **107**, 127205 (2011).
22. Halász, G. B. & Balents, L. Time-reversal invariant realization of the Weyl semimetal phase. *Phys. Rev. B* **85**, 035103 (2012).
23. Xu, S.-Y. *et al.* Discovery of a Weyl fermion semimetal and topological Fermi arcs. *Science* **349**, 613–617 (2015).
24. Lv, B. Q. *et al.* Discovery of Weyl semimetal TaAs. *Phys. Rev. X* **5**, 031013 (2015).
25. Yang, L. X. *et al.* Weyl semimetal phase in the non-centrosymmetric compound TaAs. *Nature Phys.* **11**, 728–732 (2015).
26. Xu, J. *et al.* Crystal structure, electrical transport, and magnetic properties of niobium monophosphide. *Inorg. Chem.* **35**, 845–849 (1996).
27. Chen, Y. Studies on the electronic structures of three-dimensional topological insulators by angle resolved photoemission spectroscopy. *Front. Phys.* **7**, 175–192 (2012).

Acknowledgements

Y.L.C. acknowledges support from the EPSRC (UK) grant EP/K04074X/1 and a DARPA (US) MESO project (no. N66001-11-1-4105). C.F. and B.Y. acknowledge financial support by the Deutsche Forschungsgemeinschaft DFG (Project No. EB 518/1-1 of DFG-SPP 1666 'Topological Insulators') and by the ERC Advanced Grant (No. 291472 'Idea Heusler'). Advanced Light Source is operated by Department of Energy, Office of Basic Energy Science (contract DE-AC02-05CH11231).

Author contributions

Y.L.C. conceived the experiments; Z.K.L. and L.X.Y. carried out ARPES measurements with the assistance of T.Z., H.P., H.F.Y., C.C., Y.Z. and S.-K.M.; D.P., M.S. and Y.F.G. synthesized and characterized the bulk single crystals; B.Y. and Y.S. performed *ab initio* calculations. All authors contributed to the scientific planning and discussions.

Additional information

Supplementary information is available in the [online version of the paper](#). Reprints and permissions information is available online at www.nature.com/reprints. Correspondence and requests for materials should be addressed to Y.L.C.

Competing financial interests

The authors declare no competing financial interests.

Methods

Sample synthesis. Single crystals of NbP and TaP of high quality were grown via chemical transport reaction using iodine as the transport agent. The compound NbP was first synthesized by a direct reaction of the elements niobium (Chempur 99.9%) and red phosphorus (Heraeus 99.999%) at 800 °C in evacuated fused silica tubes for 48 h. Starting from this microcrystalline powder, NbP crystallized by a chemical transport reaction in a temperature gradient from 850 °C (source) to 950 °C (sink), with a transport agent concentration of 13.5 mg cm⁻³ iodine (Alfa Aesar 99.998%). TaP is prepared using the elements tantalum (Alfa Aesar 99.9%) and red phosphorus (Heraeus 99.999%) using the same method as for NbP.

Precursor polycrystalline TaAs samples were prepared by mixing high-purity (>99.99%) Ta and As elements. The mixture was sealed into a quartz tube under high vacuum, which was then sealed into another evacuated tube for extra protection. First, the vessel was heated to 600 °C at a rate of 50 °C h⁻¹, then after 10 h of soaking it was slowly heated to 1,050 °C at a rate of 30 °C h⁻¹ and kept at this temperature for 24 h. Finally the vessel was cooled down to room temperature.

With the polycrystalline precursor, the single crystals were grown using the chemical vapour transport method in a two-zone furnace. The polycrystalline TaAs powder and 0.46 mg cm⁻³ of iodine were loaded into a 24-mm-diameter quartz tube and sealed under a vacuum. The charged part of the tube was kept at 1,150 °C and the other end at 1,000 °C for three weeks. The resulting crystals can be as large as 0.5–1 mm in size.

Angle-resolved photoemission spectroscopy. ARPES measurements were performed at beamline 10.0.1 of the Advanced Light Source (ALS) at Lawrence Berkeley National Laboratory, and beamline I05 of the Diamond Light Source (DLS). The measurement pressure was kept below 3×10^{-11} / 1.5×10^{-10} torr in ALS/DLS, and data were recorded by Scienta R4000 analysers at a sample temperature of 10 K at both facilities. The total convolved energy and angle resolutions were 16 meV/30 meV and 0.2°/0.2° at ALS/DLS, respectively. Fresh surfaces of single crystals for ARPES measurement were obtained by cleaving the sample *in situ* along its natural (001) cleavage plane.

Ab initio calculations. Electronic structures were calculated by the density functional theory (DFT) method as implemented in the Vienna *ab initio* Simulation Package (VASP). The exchange–correlation was considered in the generalized gradient approximation (GGA) and spin–orbital coupling (SOC) was included self-consistently. Experimental lattice parameters were used in the construction of a slab model with a thickness of seven unit cells to simulate a surface, in which the top and bottom surfaces are terminated by P/As and Ta/Nb, respectively. The surface band structures and Fermi surfaces were projected to the top unit cell of the P/As-terminated side, which fits the experimental band structure well. We adopted a dense k-point 400 × 400 grid in the Fermi surface calculations.